Energy & Environmental Materials WILEY

Ag-Induced Phase and Defect Engineering of Co-Evaporated Sb_2Se_3 Thin Films for Enhanced Photovoltaic Performance

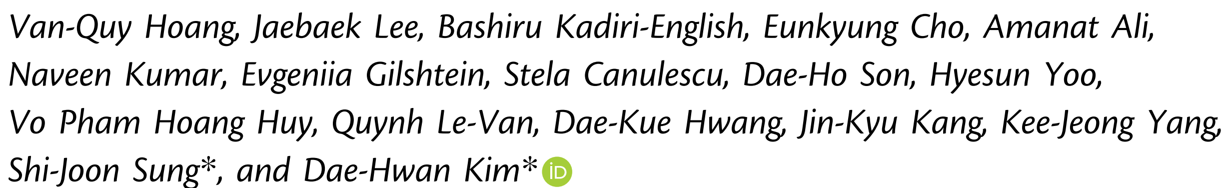

Van-Quy Hoang, Jaebaek Lee, Bashiru Kadiri-English, Eunkyung Cho, Amanat Ali, Naveen Kumar, Evgeniia Gilshtein, Stela Canulescu, Dae-Ho Son, Hyesun Yoo, Vo Pham Hoang Huy, Quynh Le-Van, Dae-Kue Hwang, Jin-Kyu Kang, Kee-Jeong Yang, Shi-Joon Sung, and Dae-Hwan Kim**

High-efficiency antimony selenide (Sb_2Se_3) solar cells remain limited by anisotropic charge transport, high defect density, and rapid back-contact recombination. We demonstrate a simple co-evaporation strategy for introducing an ultrathin Ag interlayer at the Sb_2Se_3/Mo interface. The proposed strategy significantly enhances the performance of the fabricated devices. Incorporation of an Ag layer promotes grain growth, improves crystallinity, and passivates bulk defects, thereby suppressing interfacial recombination and enhancing both the open-circuit voltage and fill factor. Structural analyses reveal an orientation transition of the quasi-one-dimensional orthorhombic Sb_2Se_3 ribbons from a preferred (hk1) orientation to a random one. This transition is driven by the sequential reaction of Ag with Se to form Ag_2Se, which subsequently reacts with Sb_2Se_3 to yield $AgSbSe_2$. However, when the Ag content exceeds the optimal level, unreacted Ag_2Se accumulates at the bottom of the film, degrading device performance. Time-resolved photoluminescence and capacitance measurements confirm reduced defect densities and optimized junction properties. The optimized Sb_2Se_3 device incorporating the Ag interlayer achieves a power conversion efficiency of 5.56%, outperforming the Ag-free counterpart under standard AM 1.5G illumination. The proposed strategy offers a promising route to high-performance Sb_2Se_3 thin-film photovoltaics and provides a pathway for tandem integration of Sb_2Se_3-based devices.

1. Introduction

Antimony selenide (Sb_2Se_3) has recently attracted considerable attention as a promising absorber material for thin-film photovoltaic applications. It exhibits several favorable properties, including a tunable indirect bandgap (1.1–1.3 eV), high absorption coefficient at visible light ($>10^5$ cm^{-1}), earth abundance, low toxicity, and intrinsic stability under ambient conditions.[1–4] Despite these advantages, the power conversion efficiency (PCE) of Sb_2Se_3-based solar cells remains relatively low compared with those of thin-film technologies, such as $Cu(In,Ga)Se_2$ (CIGS)- and $Cu_2ZnSn(S,Se)_4$-based solar cells. The reported conversion efficiency of devices is ~10.58%,[5] which is far below the Shockley–Queisser limit (~32%).[6]

The challenges limiting device performance are poor charge transport properties resulting from anisotropic crystal orientation, short carrier diffusion lengths, and morphological imperfections in the absorber layer.[7–10] To address these limitations, recent studies have focused on modifying the optical, structural, and optoelectronic properties of Sb_2Se_3 via controlled elemental substitution and optimization of processing conditions.[11–13] In particular, metal doping and alloying strategies have shown potential for enhancing the solar cell performance by tuning the band structure,[14] increasing the carrier

Dr. V.-Q. Hoang, Dr. Q. Le-Van
Center for Materials Innovation and Technology, College of Engineering and Computer Science, VinUniversity, Gia Lam district, Hanoi 14000, Vietnam
Dr. J. Lee, Dr. E. Cho, Dr. D.-H. Son, Dr. V. P. H. Huy, Dr. D.-K. Hwang, Dr. J.-K. Kang, Dr. K.-J. Yang, Dr. S.-J. Sung, Prof. D.-H. Kim
Division of Energy & Environmental Technology, Daegu-Gyeongbuk Institute of Science and Technology (DGIST), Daegu 42988, Korea
E-mail: sjsung@dgist.ac.kr
E-mail: monolith@dgist.ac.kr
B. Kadiri-English, A. Ali, Dr. S.-J. Sung, D.-H. Kim
Department of Interdisciplinary Engineering, Daegu-Gyeongbuk Institute of Science and Technology (DGIST), Daegu 42988, Korea
Dr. N. Kumar
Department of Physics, Koneru Lakshmaiah Education Foundation, Guntur 522502, India
Dr. E. Gilshtein, Prof. S. Canulescu
Department of Electrical and Photonics Engineering, Technical University of Denmark, Roskilde 4000, Denmark
Dr. H. Yoo
Regional Leading Research Center (RLRC) of Smart Energy System, Kyungpook National University, Gyeongsangbuk 37224, Korea

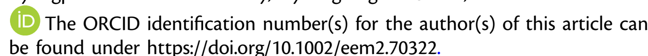

The ORCID identification number(s) for the author(s) of this article can be found under https://doi.org/10.1002/eem2.70322.

DOI: 10.1002/eem2.70322

© 2026 The Author(s). *Energy & Environmental Materials* published by John Wiley & Sons Australia, Ltd on behalf of Zhengzhou University. This is an open access article under the terms of the Creative Commons Attribution License, which permits use, distribution and reproduction in any medium, provided the original work is properly cited.

mobility,[15] and improving film quality of the absorber.[16] Among the metals, Ag has emerged as a promising dopant because of its significant influence on the structural, optical, and electrical properties of chalcogenide systems.[17–22] In CIGS-based solar cells, partial substitution of Cu by Ag has been reported to improve the optoelectronic quality.[23,24] Motivated by these findings, several studies have focused on the incorporation of dopants into the crystal lattice of Sb_2Se_3 using controlled processes.[18,22,25] Controlled incorporation of dopants into the absorber lattice prevents inhomogeneous doping or surface clustering, which are typical of solution-based techniques, and results in significant changes in optical and structural properties.

Previous studies have largely focused on Sb_2Se_3 layers doped with a limited concentration range of external elements. For example, Wang reported the synthesis of Sn-doped Sb_2Se_3 via a one-step hydrothermal process, which enhanced carrier density and charge separation, reduced surface defects, and consequently improved the photoelectrochemical performance.[11] Similarly, Cu-doped Sb_2Se_3 thin films (0–2%) deposited via thermal evaporation exhibited a decrease in optical bandgap upon Cu incorporation.[26] Guo introduced $(Sb_2Se_3)_x(AgSbSe_2)_{1-x}$ alloy films using 10 nm Ag layers, demonstrating the diffusion of Ag atoms from the back Ag contact region of the device; however, the underlying growth mechanism was not thoroughly addressed.[22]

In this study, we systematically investigated the effects of Ag incorporation over an extended concentration range and uncovered the associated growth mechanisms. We elucidated how Ag incorporation modifies the structural, morphological, compositional, and optoelectronic properties of Sb_2Se_3 films through the formation of Ag_2Se secondary and ternary $AgSbSe_2$ phases. These modifications are crucial for suppressing surface recombination and improving the heterojunction interface quality, resulting in a significant increase in device efficiency. Our findings not only advance the understanding of Ag incorporation in co-evaporated Sb_2Se_3 films but also highlight a promising route toward high-efficiency Sb_2Se_3 solar cells.

2. Results and Discussion

The Sb_2Se_3 thin films were deposited on top of sputter-deposited Ag interlayer using a co-evaporation method. The sample stacks ($Mo/Ag/Sb_2Se_3$) with different Ag interlayer thicknesses are designated as C00 (0 nm Ag), C03 (3 nm Ag), C06 (6 nm Ag), and C09 (9 nm Ag). First, the surface morphologies of the four different stacks were observed to evaluate the effect of Ag incorporation on uniformity and grain structure of the Sb_2Se_3 films. The Ag layer introduced at the Mo/Sb_2Se_3 interface formed $AgSbSe_2$ (Figure S1, Supporting Information), possibly due to interdiffusion and chemical reactions during co-evaporation.[27,28] **Figure** 1a–d shows the top-view and cross-sectional SEM images of C00 and C03, respectively, revealing distinct grain morphologies. The average grain size increases from ~300 nm in C00 to ~1.2 μm in C03, with the latter exhibiting a flatter surface and larger grains, free from the rod-like nanostructures observed in C00. Similarly, C06 and C09 films exhibit flat surfaces (Figure S2, Supporting Information). Notably, increasing Ag interlayer thickness increases the average lateral grain size, indicating that a thicker Ag interlayer promotes lateral grain growth and improves film uniformity. Cross-sectional SEM images (Figure 1c,d) reveal a clear morphological transition of the Sb_2Se_3 films from vertically aligned nanorod arrays to dense, compact thin layers. C00 exhibits the characteristic vertically oriented ribbon-like morphology of orthorhombic Sb_2Se_3, consistent with previous reports.[29–32] In contrast, C03 exhibits a more compact and uniform microstructure, lacking any rod-like nanostructures at the surface, indicating an isotropic crystal growth.

Three-dimensional (3D) atomic force microscopy (AFM) surface topographies of C00 and C03 (Figure 1e,f) show that C03 exhibits markedly lower roughness ($R_a = 19.7$ nm, $R_q = 26.4$ nm) than that of C00 ($R_a = 150.0$ nm, $R_q = 212.0$ nm), consistent with SEM observations. This indicates a transition toward a more compact and uniform morphology with enhanced crystal orientation, possibly arising from diffusion of Ag into the Sb_2Se_3 layer from the interlayer. The transition from the (hk1) orientation, characteristic of one-dimensional (1D) orthorhombic Sb_2Se_3, to random orientations attributed to the incorporation of Ag atoms into the Sb_2Se_3 lattice[22] modifies the bonding and suppresses anisotropic growth, thereby promoting isotropic and compact grain formation.[17]

Figure 1g,h show the X-ray diffraction (XRD) patterns of the Sb_2Se_3 films deposited on Ag interlayers of different thicknesses. All samples exhibit the orthorhombic crystal structure belonging to the Pbnm space group, with no noticeable impurities.[27] With increasing Ag interlayer thickness, the intensities of the (020) and (120) peaks increase, indicating that incorporation of Ag from the interlayer promotes crystal growth along the (hk0) orientation. In contrast, the intensities of the (211) and (221) peaks gradually decrease with increasing Ag interlayer thickness, implying that the presence of Ag interlayer suppresses growth along the (001) direction. The films were further characterized using grazing-incidence XRD (GIXRD) at a low incident angle (Figure S3a, Supporting Information). The peaks at 30.8° in the GIXRD patterns of C03, C06, and C09 correspond to the (200) plane of the ternary chalcogenide $AgSbSe_2$ (JCPDS: 12-0379). In the GIXRD pattern of C03, the peak related to ternary $AgSbSe_2$ can be clearly observed at an incident angle of 3°; however, its intensity decreases at 0.5°, indicating that $AgSbSe_2$ is predominantly located near the bottom of the Sb_2Se_3 film. Notably, the main (221) peak at $2\theta \approx 31.16°$ in the GIXRD patterns of C03 shifts slightly toward higher angles at different incident angles (Figure S3b, Supporting Information), indicating lattice expansion induced by Ag incorporation in the Sb_2Se_3 film from the interlayer. These results suggest that Ag incorporation into the Sb_2Se_3 lattice transforms the weakly bonded quasi-1D ribbons of Sb_2Se_3 into stronger bonded structures, thereby inhibiting (001)-oriented growth and enhancing (hk0)-oriented growth. As the binding energy of Ag–Se bonds is higher than that of Sb-Se, Ag incorporation may have enhanced the inter-ribbon connection energy and promoted growth in random orientations.[33] For the c-axis-oriented 002 and 101 peaks of C00 in Figure S4a–c, Supporting Information, the intensity distribution is skewed/nonuniform, indicating that c-axis growth occurs preferentially in localized areas where growth is particularly active. In contrast, C03 exhibits more uniform c-axis-related peak intensities, whereas the 120 and 101 peaks show a degree of preferential growth along one direction, suggesting that C03 exhibits more pronounced (hk0)-oriented growth across the film surface. The texture coefficient ($TC_{(hkl)}$) of Sb_2Se_3 films was calculated to evaluate the preferential crystallite alignment of the co-evaporated Sb_2Se_3 films using the following equation: $TC_{(hkl)} = \frac{I_{(hkl)}}{I_{0(hkl)}} / \left(\frac{1}{n} \sum_{i=1}^{n} \frac{I_{(hkl)}}{I_{0(hkl)}} \right)$, where $I_{(hkl)}$ is the measured intensity, $I_{0(hkl)}$ represents the standard intensity of the plane (hkl), and n is the number of XRD peaks considered in the calculation.[34] The obtained results indicate that the relative intensities of the hk0 peaks

© 2026 The Author(s). Energy & Environmental Materials published by John Wiley & Sons Australia, Ltd on behalf of Zhengzhou University.

25750356, 0, Downloaded from https://onlinelibrary.wiley.com/doi/10.1002/eem2.70322 by Daegu Gyeongbuk Institute Of, Wiley Online Library on [09/04/2026]. See the Terms and Conditions (https://onlinelibrary.wiley.com/terms-and-conditions) on Wiley Online Library for rules of use; OA articles are governed by the applicable Creative Commons License

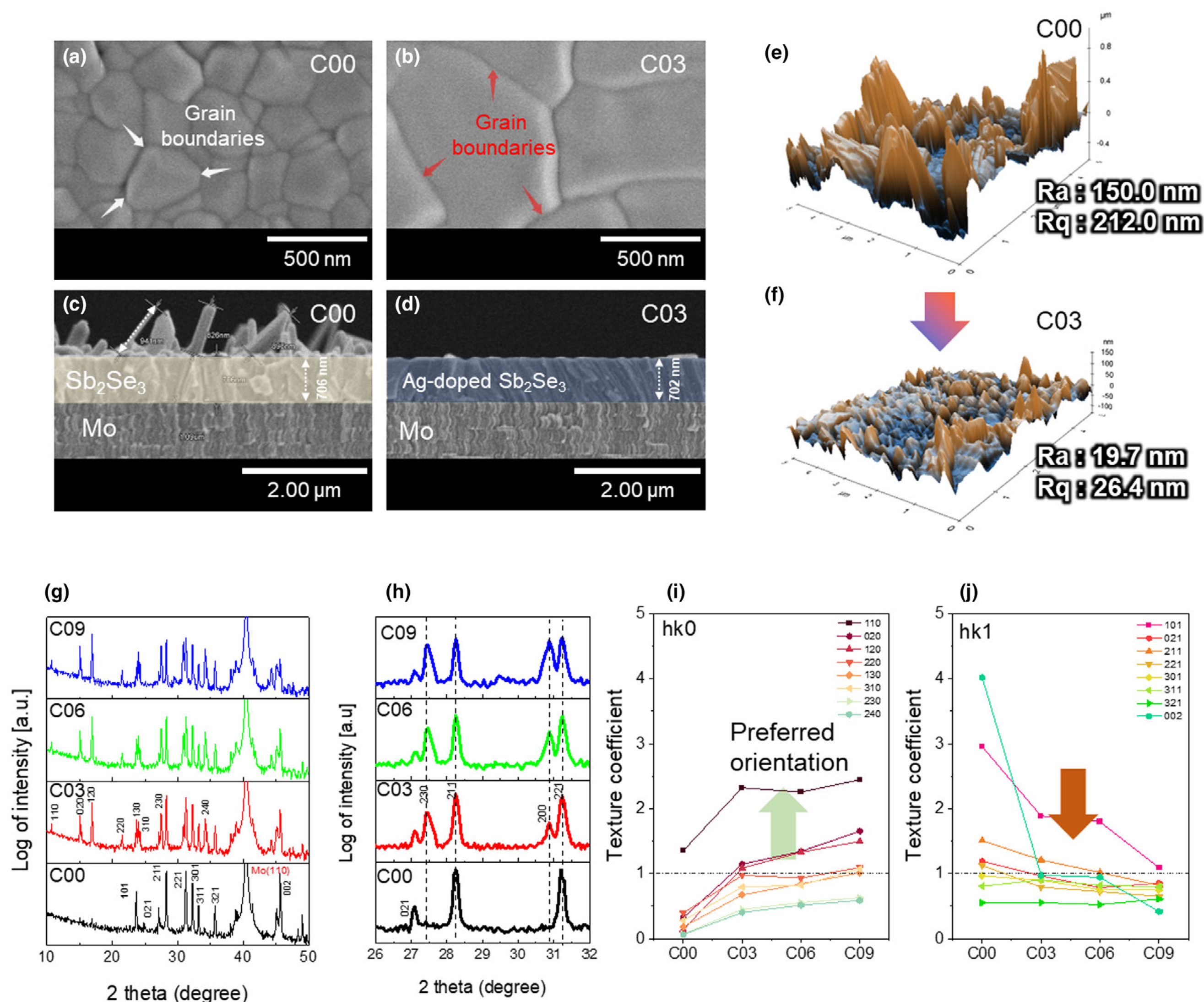

Figure 1. Morphological and structural characterization of Sb_2Se_3 films deposited on Ag interlayers with different thicknesses. a–d) Top-view and cross-sectional SEM images showing grain structure evolution without Ag (C00) and with a 3 nm Ag interlayer (C03). e, f) 3D AFM surface topographies of C00 and C03, respectively, highlighting differences in surface uniformity. XRD patterns in the 2θ range of g) 10–50° and h) 26–32°. i, j) texture coefficients of co-evaporated Sb_2Se_3 thin films showing phase evolution and preferred orientation (the arrows) with increasing Ag content.

increase (Figure 1i), whereas those of hk1 peaks decrease (Figure 1j) with increasing Ag interlayer thickness. To summarize, Ag interlayer facilitates preferential Sb_2Se_3 growth along the (hk0) orientation through the formation of a 3D $AgSbSe_2$ crystal structure while suppressing the growth of Sb_2Se_3 nanoribbons oriented perpendicular to the substrate.[27]

Figure 2a shows the Raman spectra of the examined absorber layers. All Sb_2Se_3 samples exhibit three characteristic peaks at 190, 210, and 253 cm^{-1}, corresponding to the orthorhombic Sb_2Se_3 phase.[35] With increasing Ag interlayer thickness, additional low-intensity Raman active bands at 117 and 371 cm^{-1} appear in C06 and C09, which can be attributed to the formation of the ternary $AgSbSe_2$ phase, consistent with the XRD results.[36,37] In contrast, in C03, these two weak bands are absent, likely because the incorporated Ag content is insufficient to form a detectable amount of $AgSbSe_2$.

To better understand the chemical composition of the examined Sb_2Se_3 films, X-ray photoelectron spectroscopy (XPS) analyses were performed on C00 and C03 after surface etching for 40 s. The peaks at 529.80 and 539.12 eV observed in the Sb 3d spectrum of C00 (Figure 2b) correspond to Sb $3d_{5/2}$ and Sb $3d_{3/2}$, respectively. The peaks at 530.06 and 539.44 eV observed in the Sb 3d spectrum of C03 indicate the formation of a new compound, $AgSbSe_2$, corroborating the XRD data.

In the Se 3d spectra (Figure 2c), a shoulder at higher binding energy, obtained after fitting Se 3d region with two doublets, is observed for both C00 and C03. Moreover, for both C00 and C03, the Se $3d_{5/2}$ peak is observed within the binding range 54.3–57.3 eV. As Ag is less electronegative than Sb, the Se atoms bonded to Ag experience an increase in electron density and become more negatively charged, leading to a reduction in binding energy, consistent with the

© 2026 The Author(s). *Energy & Environmental Materials* published by John Wiley & Sons Australia, Ltd on behalf of Zhengzhou University.

25750356, 0, Downloaded from https://onlinelibrary.wiley.com/doi/10.1002/eem2.70322 by Daegu Gyeongbuk Institute Of, Wiley Online Library on [09/04/2026]. See the Terms and Conditions (https://onlinelibrary.wiley.com/terms-and-conditions) on Wiley Online Library for rules of use; OA articles are governed by the applicable Creative Commons License

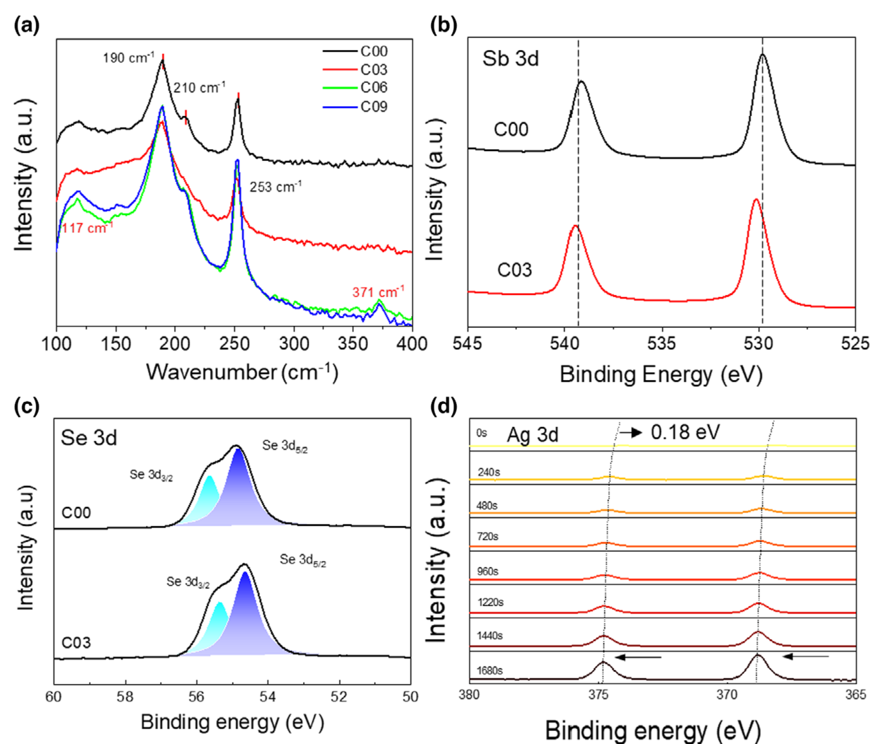

Figure 2. a) Raman spectra of Sb_2Se_3 films deposited on Ag interlayers with different thicknesses. Raman peaks at 117 and 371 cm^{-1}, highlighted in red, correspond to the formation of the ternary $AgSbSe_2$ phase. b) Sb 3d and c) Se 3d X-ray photoelectron spectroscopy (XPS) spectra of C00 and C03 films after sputter etching. d) High-resolution Ag 3d XPS spectra of C03 showing a shift toward low binding energy due to Ag incorporation at different etching depths.

observed binding-energy shift in the XPS spectra. The Se 3d XPS spectra reveal binding-energy shifts upon Ag incorporation; shifts toward lower binding energies indicate changes in the local bonding environment due to lattice strain or compression induced by incorporated Ag atoms in the Sb_2Se_3 lattice. These observations indicate that Ag incorporation significantly modifies the bulk structure, surface chemistry, and electronic states of Sb_2Se_3 films.

The interaction between Ag and Sb_2Se_3 during co-evaporation was investigated by performing depth-resolved XPS on C03. Figure 2d indicates that Ag is incorporated into the Sb_2Se_3 lattice, adopting a more ionic form (Ag^+ in $AgSbSe_2$), resulting in a higher binding-energy shift owing to the lower electron density around Ag in Sb_2Se_3 compared to that around Ag in its own lattice. Depth-resolved XPS analysis reveals that Ag atoms diffuse into Sb_2Se_3, forming stronger bonds and causing binding-energy shifts. When Ag substitutes for Sb via substitutional doping, the local charge distribution is altered, resulting in a higher binding energy.[38] The Ag 3d spectrum of C09 (Figure S5, Supporting Information) obtained after 1680 s of etching shows two peaks ($3d_{5/2}$ and $3d_{3/2}$) shifted by 0.53 eV, relative to the XPS peaks obtained from the surface. The observed shift in the Ag 3d peaks for C09 is higher than those for C03 (0.18 eV) and C06 (0.36 eV), respectively. Although the XRD results did not indicate the formation of an Ag_2Se secondary phase in C03, the XPS-derived binding-energy values closely matched those reported for this phase.[39,40] Depth profile analysis further reveals an increasing Ag concentration with depth, accompanied by a corresponding shift toward higher Ag binding energies, possibly due to the formation of $AgSbSe_2$ in regions of high Ag content.

Ultraviolet photoelectron spectroscopy (UPS) was used to determine the electronic band structure of the films (**Figure 3**a). The valence band edge (E_v) and work function (φ) of the absorber films were extracted from the UPS spectra (Figure S6, Supporting Information). UPS analysis revealed that both the valence and conduction band edges of Sb_2Se_3 shift upward upon Ag incorporation, resulting in a reduced conduction band offset and an increased valence band offset with CdS. This modification leads to a more favorable energy-level alignment for charge transport. In the Ag-incorporated Sb_2Se_3 films, the conduction band offset with CdS becomes nearly zero, which is advantageous for efficient electron extraction while suppressing interfacial recombination. Furthermore, the enlarged valence band offset effectively blocks hole leakage from the absorber into the buffer layer, thereby reducing interfacial recombination. Additionally, the decreased separation between the Fermi level and valence band maximum indicates an enhanced p-type character, suggesting improved junction formation.

As Ag dopants reconstruct the Sb_2Se_3 surface, they can directly impact the recombination behavior at the PN junction; therefore, time-resolved photoluminescence (TRPL) was used to evaluate the minority carrier lifetimes. Figure 3b shows the TRPL-derived minority carrier lifetimes of the absorber layers (C00, C03, C06 and C09), with the curves fitted using a multi-exponential function: $y = A_1 e^{-t/\tau_1} + A_2 e^{-t/\tau_2} + A_3 e^{-t/\tau_3} + A_4 e^{-t/\tau_4}$, where τ_1, τ_2, τ_3, and τ_4 represent the decay components, and A_1, A_2, A_3, and A_4, are the corresponding amplitude coefficients. The decay lifetimes τ_1 and τ_2 correspond to the fast decay components, which are generally attributed to surface or interface recombination and trap-assisted nonradiative recombination processes (**Table 1**). These fast components reflect how quickly carriers recombine or are extracted near defects or interfaces. On the other hand, τ_3 and τ_4 represent the slow decay components, typically associated with bulk recombination of carriers in the absorber material. These slower lifetimes correspond to recombination of minority carriers in relatively defect-free regions, thus reflecting the intrinsic carrier lifetime within the bulk of the absorber. Ag-incorporated Sb_2Se_3 absorber layers exhibit longer carrier lifetimes than those exhibited by the pure film (C00: 2.9 ns; C03: 3.2 ns; C06: 4.9 ns; and C09: 3.6 ns). The prolonged carrier recombination lifetime observed for the Ag-incorporated films indicate that the reduction in nonradiative recombination is due to the improved crystallinity and reduced defects within the Sb_2Se_3 layer.[41] The variations in these average lifetimes correlate closely with microstructural changes observed by XRD and SEM, such as improved crystallinity and preferred orientation, which reduce defect density and enhance carrier transport. Thus, longer average lifetimes of Ag-incorporated samples indicate better bulk quality and suppressed nonradiative recombination, while shorter lifetimes suggest more recombination at defects or interfaces. Carrier extraction was investigated by performing TRPL measurements on the complete devices (see Table S1, Supporting Information). Analysis of carrier extraction performance,

© 2026 The Author(s). Energy & Environmental Materials published by John Wiley & Sons Australia, Ltd on behalf of Zhengzhou University.

25750356, 0, Downloaded from https://onlinelibrary.wiley.com/doi/10.1002/eem2.70322 by Daegu Gyeongbuk Institute Of, Wiley Online Library on [09/04/2026]. See the Terms and Conditions (https://onlinelibrary.wiley.com/terms-and-conditions) on Wiley Online Library for rules of use; OA articles are governed by the applicable Creative Commons License

25750356, 0, Downloaded from https://onlinelibrary.wiley.com/doi/10.1002/eem2.70322 by Daegu Gyeongbuk Institute Of, Wiley Online Library on [09/04/2026]. See the Terms and Conditions (https://onlinelibrary.wiley.com/terms-and-conditions) on Wiley Online Library for rules of use; OA articles are governed by the applicable Creative Commons License

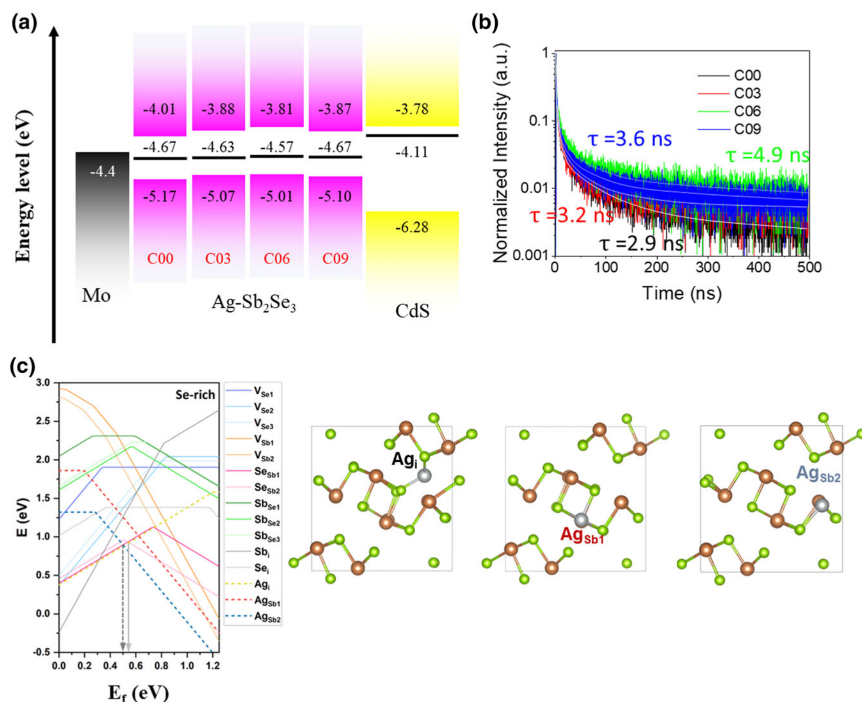

Figure 3. a) Band alignment at the CdS/Sb_2Se_3 (Ag-incorporated or pure) absorber heterointerfaces. b) TRPL spectra of C00, C03, C06 and C09. c) Calculated formation energies of intrinsic defects (solid lines) and Ag-related defects (dashed lines) in absorber layers under Se-rich conditions as a function of Fermi energy (E_f), along with Sb_2Se_3 structures containing Ag-related defects. The solid and dashed gray arrows indicate the calculated Fermi energy levels in Sb_2Se_3 and Ag-incorporated Sb_2Se_3, respectively.

Table 1. PL lifetime obtained from fitted TRPL decay and average lifetime of Sb_2Se_3 samples.

Samples	A_1 (%)	τ_1 (ns)	A_2 (%)	τ_2 (ns)	A_3 (%)	τ_3 (ns)	A_4 (%)	τ_4 (ns)	τ_{aver} (ns)
C00	35.0	0.29	77.7	2.7	21.80	17	4.9	129	2.9
C03	12.0	0.43	29.3	3.0	7.59	18	1.7	137	3.2
C06	60.4	0.46	22.5	3.1	7.90	15	2.0	114	4.9
C09	10.1	0.45	36.7	2.8	10.27	15	2.5	110	3.6

based on the lifetimes in C00 and C03, shows that τ_1 decreases by 31.5% while τ_2 decreases by only 3.7%. This explains the more pronounced decrease in $\tau_{avg,(Amplitude)}$ than that in $\tau_{avg,(Intensity)}$, indicating that interfacial or surface charge transfer (extraction) is accelerated.

Density functional theory (DFT) calculations were performed at the HSE06-D3(BJ) level to better understand the effects of Ag incorporation on the electronic and structural properties of Sb_2Se_3 under Se-rich growth conditions. All possible defect configurations, including interstitial Ag (Ag_i) and Ag substitution at Sb sites (Ag_{Sb1} and Ag_{Sb2}), along with relevant intrinsic defects were considered. Detailed computational methodologies are described in our previous work.[42] As shown in Figure 3c, Ag_{Sb2} exhibits the lowest formation energy among Ag-related defects, suggesting that Ag preferentially occupies the Sb2 lattice site and acts as an acceptor, contributing to the increased hole carrier concentration. The calculated Fermi level of Ag-assisted Sb_2Se_3 under charge neutrality is 0.51 eV, which is slightly lower than that of C00 (0.54 eV), indicating a slight increase in p-type conductivity upon Ag incorporation. Notably, the favorable formation of the acceptor Ag_{Sb2} potentially suppresses the generation of native deep-level defects, thereby reducing deep-level recombination and further enhancing charge carrier transport in the Sb_2Se_3 layer of the device.

To elucidate the compositional and interfacial modifications induced by Ag incorporation into Sb_2Se_3, correlative depth-resolved cross-sectional characterization was performed using time-of-flight secondary ion mass spectrometry (ToF-SIMS) and 3D elemental mapping (**Figure 4a–h**). In C00, the ToF-SIMS profile (Figure 4a) and 3D elemental reconstruction (Figure 4e) reveal the uniform presence of Sb. Back-diffusion of Sb into the back Mo electrode is detrimental because it drives the formation of Mo–Sb interfacial alloys that introduce active sites for recombination. Mo–Sb interfacial alloys exhibit higher resistivity compared with that exhibited by metallic Mo,[34] increasing the series resistance (R_s) of the device. In the Ag-incorporated Sb_2Se_3 samples, the formation of the ternary $AgSbSe_2$ phase suppresses Sb diffusion into the Mo substrate, thereby enabling efficient charge transport across the back contact and reducing R_s. Meanwhile, the mitigation of interfacial defects and leakage pathways strengthens the junction integrity, resulting in a higher shunt resistance (R_{sh}) and improved device efficiency. For C06 and C09, the SIMS data from Figure 4c,d show an unchanged Ag depth profile, with a plateau extending from the front side to the middle of the films, indicating that Ag atoms diffused through the bulk to form the ternary $AgSbSe_2$ phase. Moreover, the average intensity of Ag in this plateau region, compared with the intensities of Sb and Se, increases with increasing Ag interlayer thickness, indicating the diffusion of more Ag atoms into the bulk. In addition, Ag accumulation near the back Mo contact in all films indicates that the in-depth distribution of Ag is not entirely homogeneous, consistent with the results of the 3D elemental mapping (Figure 4g,h). Achieving a uniform distribution of Ag is challenging because Ag is introduced from the bottom of the device stack, which is processed at relatively low temperatures.

To further investigate the formation of secondary Ag_2Se and ternary $AgSbSe_2$ phases, the samples were analyzed using scanning transmission electron microscopy (STEM) combined with energy-dispersive X-ray spectroscopy (EDS). Figure 4i–l shows the EDS maps showing distributions of Ag in Sb_2Se_3 films deposited on Ag interlayers with different thicknesses. For C03 sample, the Ag concentration was too low to be determined using STEM-EDS analysis, although Ag appeared to be uniformly distributed. SIMS depth profiling revealed that Ag is more concentrated toward the back interface. For C06 and C09, a distinct Ag signal is observed at the Sb_2Se_3/Mo interface, indicating the formation of an approximately 200 nm-thick Ag_2Se pyramid-like structure, as confirmed by TEM analysis (Figure S7, Supporting Information). A significant reduction in Sb-related signals arising from near the back interface further supports the formation of an Ag_2Se secondary phase,

© 2026 The Author(s). Energy & Environmental Materials published by John Wiley & Sons Australia, Ltd on behalf of Zhengzhou University.

25750356, 0, Downloaded from https://onlinelibrary.wiley.com/doi/10.1002/eem2.70322 by Daegu Gyeongbuk Institute Of, Wiley Online Library on [09/04/2026]. See the Terms and Conditions (https://onlinelibrary.wiley.com/terms-and-conditions) on Wiley Online Library for rules of use; OA articles are governed by the applicable Creative Commons License

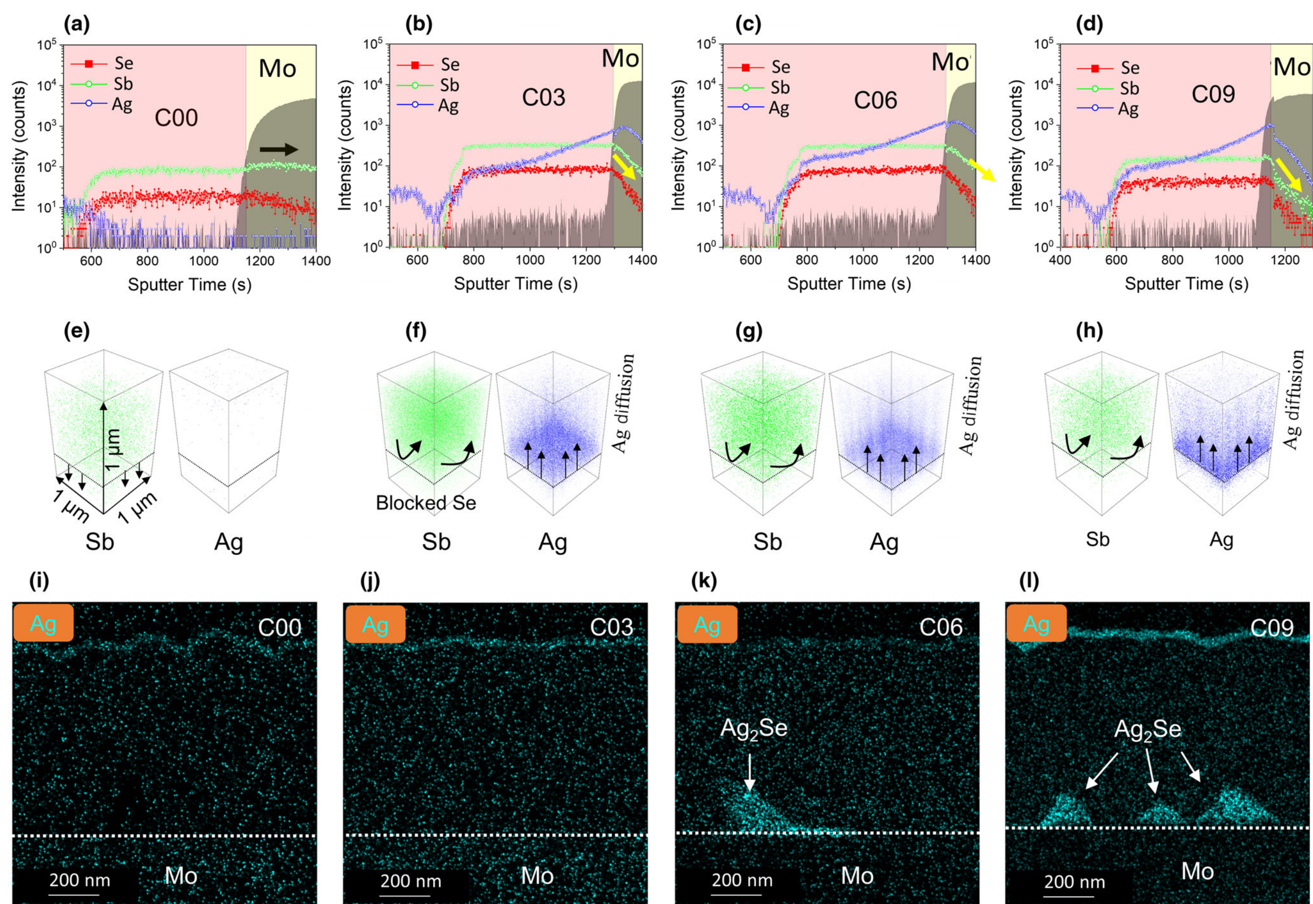

Figure 4. a–d) TOF-SIMS depth profiles, e–h) 3D ToF-SIMS elemental mapping images of Sb and Ag, and i–l) cross-sectional EDS maps showing distributions of Ag in Sb_2Se_3 films deposited on Ag interlayers with different thicknesses: C00, C03, C06, and C09.

consistent with the Ag 3d XPS data (see Figure S8, Supporting Information). The Ag distributions observed using EDS line scans are consistent with the SIMS depth profiles (Figure 4a–d) and cross-sectional TEM-EDS maps, showing Ag accumulation at the Mo/Sb_2Se_3 interface. Agreement among the results obtained using different characterization techniques supports the conclusion that Ag accumulation at the Mo/Sb_2Se_3 interface of C06 and C09 depends on the diffused Ag concentration in the absorber layer, underscoring the key role of Ag interlayer in modifying the back interface. We posit that the growth mechanism of the Ag-incorporated Sb_2Se_3 layer is mainly influenced by a sequential reaction pathway that possibly operates during Ag-incorporated Sb_2Se_3 film growth. Initially, Ag reacts with Se to form Ag_2Se, which subsequently undergoes solid-state exchange with Sb_2Se_3 to produce a thin $AgSbSe_2$ alloy layer at the substrate interface. This cubic layer suppresses the natural 1D ribbon-like growth of Sb_2Se_3, promoting the development of a disordered, two-dimensional morphology. As growth proceeds, Sb_2Se_3 nucleates and extends on top of the $AgSbSe_2$ layer while Ag_2Se remains concentrated near the back interface owing to the limited reaction temperature. The pre-deposited Ag enhances the film density and reduces defects; however, excessive Ag incorporation leads to the formation of randomly oriented Sb_2Se_3 ribbons that hinder efficient carrier extraction. Therefore, only a small amount of Ag (<3 nm) incorporation in Sb_2Se_3 films is beneficial.

The effects of Ag incorporation into the absorber layer on device performance were systematically investigated. Comparison of complete devices based on C00 and C03 (**Figure 5**a–g) shows that the efficiency increases from 3.09% to 5.56%, mainly due to increases in V_{OC} (from 292.76 to 374.54 mV) and fill factor (FF) (from 38.14% to 55.42%). Equally important is the development of highly reproducible co-evaporated Sb_2Se_3 with minimal efficiency deviation among devices. To achieve high-yield co-evaporated Sb_2Se_3 solar cells, effective control of the interfacial quality between the Sb_2Se_3 light-absorbing layer and the CdS buffer layer is critical. The increase in FF can be attributed to originate from the denser absorber morphology, which suppresses shunt leakage paths, and the increase in V_{OC} can be attributed to originate from the combined effects of a slightly widened bandgap and reduced nonradiative recombination (Figure 5h,i and **Table 2**). In addition, the low conversion efficiency of chalcogenide-based solar cells is primarily limited by the large voltage deficit ($V_{OC\text{-def}}$).[43] We have further calculated the $V_{OC\text{-def}}$ to intuitively assess V_{OC}. The efficient reduction of $V_{OC\text{-def}}$ values from 869.2 mV (C00) to 815.4 mV (C03) is mainly due to the significantly inhibited nonradiative recombination and defect states, which are commonly related to the morphology and crystallinity of Sb_2Se_3 films (see the discussion below).[44] Notably, the FF exceeding 50% achieved in this study is higher than those reported for other high-efficiency Sb_2Se_3 solar cells on Mo substrates fabricated via co-

© 2026 The Author(s). *Energy & Environmental Materials* published by John Wiley & Sons Australia, Ltd on behalf of Zhengzhou University.

25750356, 0, Downloaded from https://onlinelibrary.wiley.com/doi/10.1002/eem2.70322 by Daegu Gyeongbuk Institute Of, Wiley Online Library on [09/04/2026]. See the Terms and Conditions (https://onlinelibrary.wiley.com/terms-and-conditions) on Wiley Online Library for rules of use; OA articles are governed by the applicable Creative Commons License

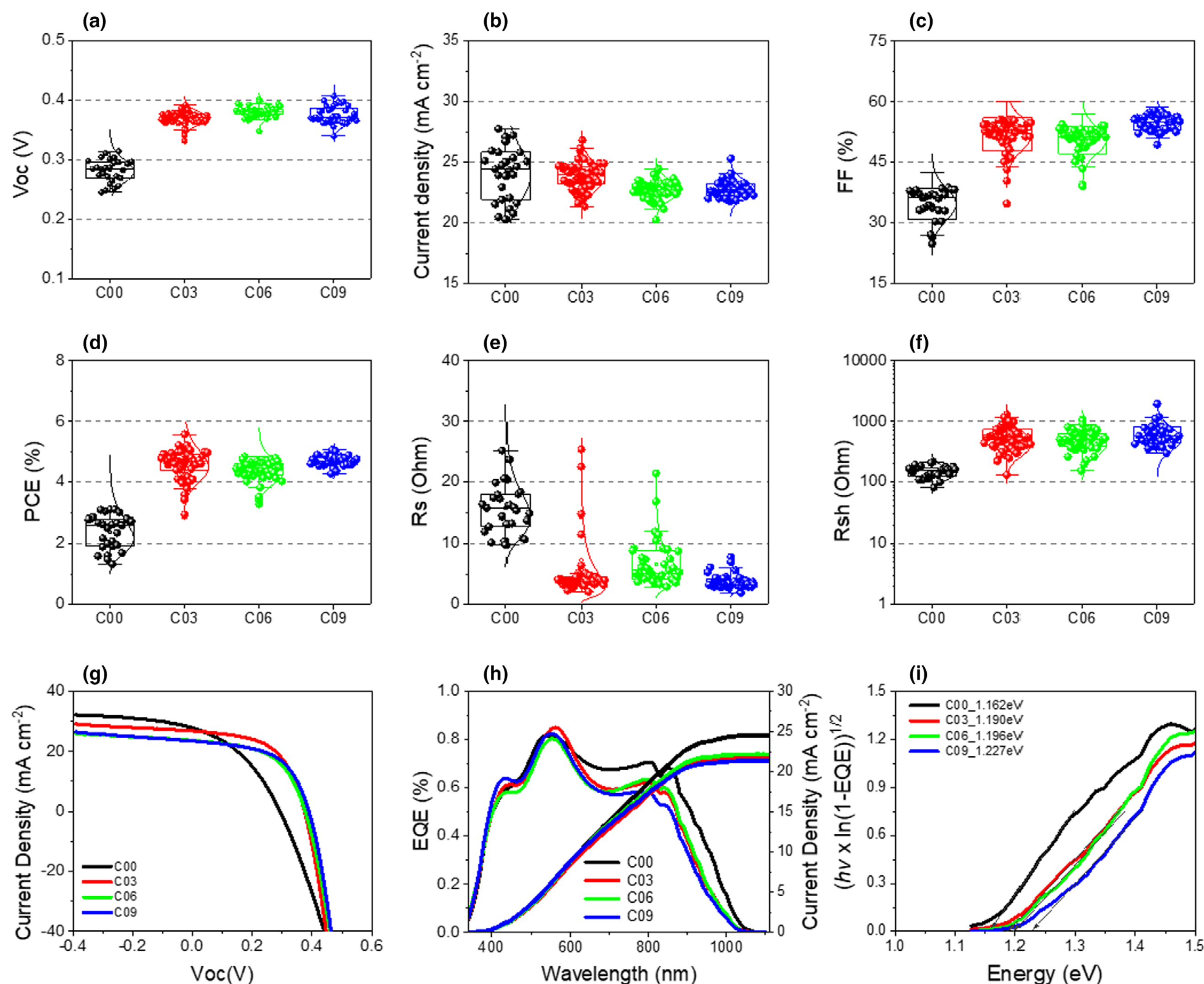

Figure 5. a–f) Statistical box plots of the photovoltaic parameter of cells with Sb_2Se_3 absorber layers deposited on Ag interlayers with different thicknesses. g) Current density–voltage curves of the solar cells under the standard AM 1.5G illumination. h) EQE spectra. i) Bandgaps determination plots obtained EQE spectra.

Table 2. Photovoltaic parameters of solar cells with Sb_2Se_3 absorber layers deposited on Ag interlayers with different thicknesses, measured under 1 Sun AM 1.5G illumination.

Samples	V_{OC} (mV)	J_{SC} (mA cm^{-2})	FF (%)	PCE (%)	R_s (Ωsq^{-1})	R_{sh} (Ωsq^{-1})	E_g (V)	$V_{OC\text{-}def}$ (mV)	Enhancement in V_{OC} (%)
C00	292.76	27.75	38.14	3.09	10.70	164.80	1.162	869.2	–
C03	374.54	26.82	55.42	5.56	3.20	439.80	1.190	815.4	27.93
C06	376.83	23.53	54.40	4.82	3.80	262.20	1.196	819.1	27.76
C09	389.05	23.41	55.50	5.05	2.90	488.60	1.227	837.9	32.89

evaporation. In contrast to the increases in FF and V_{OC}, J_{SC} values show a slight decrease in Ag-incorporated devices, consistent with reduced external quantum efficiencies (EQEs) at longer wavelengths observed for C03, C06, and C09 compared to those observed for C00. This observation can be explained by the bandgap widening that narrows the absorption range. Although the lack of (hk1)-orientated lattice planes in the Sb_2Se_3 absorber layer hinders carrier transport, Ag incorporation enhances device stability by promoting a denser morphology, improving p-type conductivity, and enabling more favorable band alignment. Therefore, developing strategies to promote the (hk1)-

© 2026 The Author(s). *Energy & Environmental Materials* published by John Wiley & Sons Australia, Ltd on behalf of Zhengzhou University.

orientated growth, combined with positive effects of Ag incorporation, can result in a synergistic effect that can further enhance the overall device efficiency. The corresponding electrical behaviors of solar cells, with different Ag concentrations in the Sb_2Se_3 absorber layer, are shown in Figure S9, Supporting Information. The Sb_2Se_3 solar cell fabricated by co-evaporated method exhibited the highest current density, attributed to the hk1 preferred orientation. In contrast, Ag-incorporated Sb_2Se_3 yielded a pronounced V_{OC}, because of the defect's passivation, achieving the highest efficiency under the optimal condition of 3 nm Ag. We analyzed a graph plotting ln ($J + J_{SC}$-GV) against V-RJ to identify the factors of series and shunt resistances. The saturation current density (J_0) decreased from 0.341 mA cm^{-2} (C00) to 0.096 mA cm^{-2} (C03). Specifically, plots of dV/dJ versus $(J + J_{SC})^{-1}$ and dJ/dV versus voltage (V) were examined to assess the average shunt conductance and series resistance. The Ag-incorporated Sb_2Se_3 device demonstrated lower parasitic losses culminating in higher V_{OC} and FF, and ultimately, superior device performance.

Various defects can arise in the Sb_2Se_3 absorber layer, including vacancies, interstitials, and defect clusters. These defects introduce specific energy levels within the bandgap (E_g) and function as donor or acceptor defects. The energy levels of these defects significantly impact the device performance, as they often serve as recombination centers for electron–hole pairs. Admittance spectroscopy (AS) provides information on the energy levels and densities of acceptor defects near the space charge region (SCR). Therefore, understanding the elemental variations near the SCR is essential for investigating these defects. **Figure 6a–d** shows the capacitance spectra obtained from the four representative Sb_2Se_3 devices at temperatures ranging from 130 to 300 K in 10 K increments. AS analysis shows that Ag incorporation into the Sb_2Se_3 absorber layer modifies the originally present defects. The C03-based device exhibits an optimal doping level (Ag incorporation), which minimizes deep trap states and enhances junction quality, as revealed by a more uniform and faster thermal response in the low-frequency region ($<10^5$ Hz). The overall trend across all devices highlights the role of Ag incorporation in effectively passivating the undesired defects and modulating the carrier density. Furthermore, the incorporation of Ag into the absorber layer promotes the formation of a uniform $AgSbSe_2$ surface, thereby enhancing the quality of the p–n junction and effectively suppressing interfacial charge recombination.

Next, AS was employed to characterize the charged defects near the SCR. From the AS curves (Figure 6a–d), the activation energy (E_a) relative to the valence band edge (E_v) was determined using Arrhenius plots (Figure 6e–h). Each Arrhenius plot was constructed according to the relation: $\omega_0 = 2\pi\nu_0 T_2 \exp(-E_a/kT)$, where ω_0 is the inflection point of the capacitance function, ν_0 is the pre-exponential factor, T is the Kelvin temperature, and k is the Boltzmann constant. The estimated defect concentrations and activation energies, and other device parameters are summarized in **Table 3**. The Arrhenius plots of the Sb_2Se_3-based solar cells were obtained by plotting ln(current) versus 1/T, showing linear temperature dependence. The slope of the linear fit in

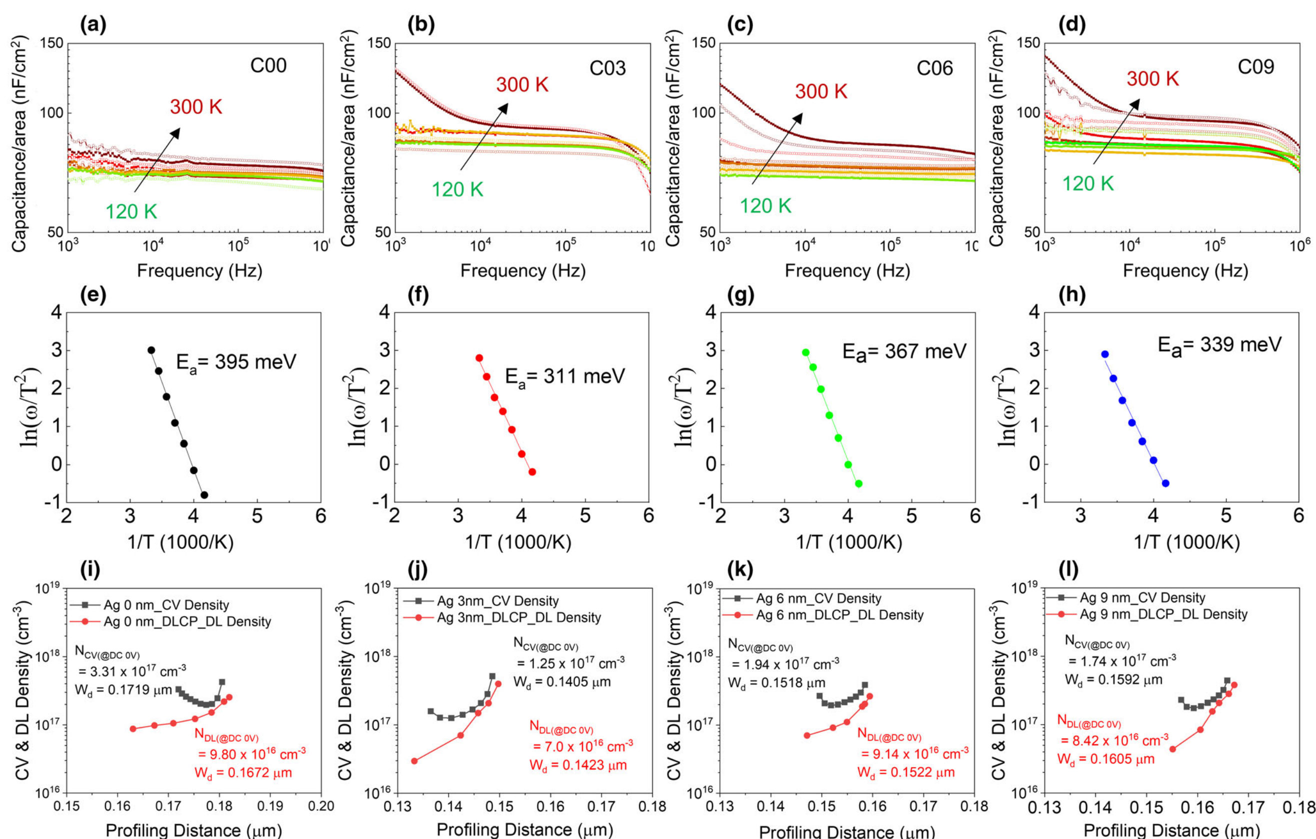

Figure 6. Defect characteristics of solar cells with Sb_2Se_3 absorber layer (C00, C03, C06, and C09). a–d) Results of AS measurements performed at temperatures ranging from 120 to 300 K. e–h) Arrhenius plots of the inflection points of the capacitance function for solar cells incorporating C00, C03, C06, or C09, derived from the AS data. E_a corresponds to the main defect energy level within the absorber layer. i–l) N_{CV} and N_{DL} density curves at 300 K for all samples.

© 2026 The Author(s). *Energy & Environmental Materials* published by John Wiley & Sons Australia, Ltd on behalf of Zhengzhou University.

25750356, 0, Downloaded from https://onlinelibrary.wiley.com/doi/10.1002/eem2.70322 by Daegu Gyeongbuk Institute Of, Wiley Online Library on [09/04/2026]. See the Terms and Conditions (https://onlinelibrary.wiley.com/terms-and-conditions) on Wiley Online Library for rules of use; OA articles are governed by the applicable Creative Commons License

Table 3. Summary of parameters obtained using admittance spectroscopy, capacitance–voltage, and deep-level transient capacitance profiling measurements for Ag-incorporated Sb_2Se_3 solar cells corresponding to the best-performing device at each Ag concentration.

Samples	N_{CV} (cm^{-3})	N_{DL} (cm^{-3})	N_{IT} (cm^{-3})	V_{bi} (V)	W_d (μm)	E_a (meV)
C00	3.31×10^{17}	9.80×10^{16}	2.33×10^{17}	0.336	0.1719	395
C03	1.25×10^{17}	7.00×10^{16}	5.50×10^{16}	0.440	0.1405	311
C06	1.94×10^{17}	9.14×10^{16}	1.03×10^{17}	0.405	0.1518	367
C09	1.74×10^{17}	8.42×10^{16}	8.98×10^{16}	0.424	0.1592	339

an Arrhenius plot corresponds to the E_a of the defect responsible for charge transport. For C00, C03, C09, and C06 (Figure 6e), the activation of the main deep acceptor defects is determined to be 395, 311, 339, and 367 meV, respectively, indicating that Ag incorporation into the absorber layer creates favorable conditions for carrier transport by reducing transport barriers and minimizing recombination losses. A lower E_a facilitates easier charge transport, decreases recombination barriers, reduces R_s, lowers interface trap densities, and enhances overall device efficiency.[45]

The results of EDS (Figure 4i–m) and GIXRD (Figure S4, Supporting Information) analyses confirm the presence of Ag in the Sb_2Se_3 absorber layer near the SCR. The determined energies of the main acceptor levels (Figure 6e–h) indicate the presence of various defects, including Sb vacancies (V_{Sb}), antisite defects with Sb atom on a Se site (Sb_{Se}), and defect complexes involving both Sb and Se vacancies ($V_{Sb} + V_{Se}$), near the SCR of C00.

To elucidate the impact of Ag incorporation on the electronic properties and defect chemistry of the Sb_2Se_3 devices, capacitance–voltage (C–V) and deep-level transient capacitance profiling analyses were conducted. Figure 6i–l clearly shows that the introduction of Ag into the absorber layer modulates both the junction characteristics and defect densities in a systematic and beneficial manner. C–V profiling indicates that the extracted (apparent) carrier density is largely governed by the trap states at the Sb_2Se_3/CdS interface. The total carrier concentration (N_{CV}) comprises both interfacial (N_{IT}) and bulk (N_{DL}) contributions, expressed as: $N_{IT} = N_{CV} - N_{DL}$. A Mott–Schottky plot was derived from the C–V data by plotting $1/C^2$ against the applied voltage (V), and the slope of the linear region was used to calculate the built-in potential (V_{bi}) (Figure S10, Supporting Information). The C00 device exhibits a relatively high N_{CV} of 3.31×10^{17} cm^{-3}, with a V_{bi} of 0.336 V. The C00 device also exhibits a high N_{IT} of 2.33×10^{17} cm^{-3}, indicating a large density of electrically active defects at the junction. The C03 device exhibits a relatively lower N_{CV} of 1.25×10^{17} cm^{-3} and N_{IT} of 5.50×10^{16} cm^{-3}, indicating an early-stage passivation effect. Interestingly, the C06 device represents a transitional stage in which interfacial Ag begins to accumulate, as corroborated by SIMS and EDS results (Figure 4). The C06 device exhibits relatively higher N_{CV} of 1.94×10^{17} cm^{-3} and moderate N_{IT} of 1.03×10^{16} cm^{-3}, indicating enhanced doping alongside persistent interface-related defects. The C06 device reflects partial structural and electronic modification, where Ag begins to improve the junction characteristics but has not yet fully optimized the interface. The C09 device exhibits the highest N_{CV} of 1.74×10^{17} cm^{-3}, indicating an enhanced junction potential. This improvement facilitates more efficient charge carrier separation, reduces bulk and interface recombination, increases V_{OC}, and enhances the FF by lowering the leakage currents, ultimately enhancing the overall device efficiency. Notably, N_{DL} increases moderately to 8.42×10^{16} cm^{-3} while N_{IT} decreases to 8.98×10^{16} cm^{-3}, reflecting substantial passivation of interfacial and bulk defects. These results are consistent with the formation of $AgSbSe_2$, which improves band alignment and carrier collection while mitigating deep-level recombination.

3. Conclusion

This study demonstrated that introducing an ultrathin Ag interlayer at the Sb_2Se_3/Mo interface offers a simple yet powerful route for simultaneously engineering both the bulk and interface properties of Sb_2Se_3-based solar cells. The incorporation of the Ag interlayer promoted better grain growth and improved crystallinity of the Sb_2Se_3 layer, although the crystalline orientation was affected by the different growth kinetics of the co-evaporated Sb_2Se_3 thin films containing different amounts of Ag incorporated from the interlayer. The Ag interlayer with a thickness of 3 nm effectively passivated deep defects via controlled Ag incorporation into the Sb_2Se_3 absorber layer and improved the back-contact band alignment while suppressing the formation of detrimental Ag_2Se secondary phases. Solar cells based on Ag-incorporated Sb_2Se_3 absorber layer achieved an excellent PCE of 5.56%, which is considerably higher than that of the solar cells based on pure Sb_2Se_3 (PCE: 3.09%). This study not only advances the fundamental understanding of Ag interlayer-mediated growth of co-evaporated Sb_2Se_3 films but also establishes a practical pathway to boost efficiency and facilitate the future tandem integration of co-evaporated Sb_2Se_3-based solar cells. Future research could focus on addressing the current limitations by exploring post-deposition Ag treatments on the top of the Sb_2Se_3 layer or further reducing the Ag content to achieve better control of Ag diffusion, thereby minimizing secondary phase formation and enhancing device's performance.

4. Experimental Section

Device fabrication: *Ultrathin Ag layer*—A Mo back electrode with a thickness of 900 nm was prepared onto the soda–lime glass (SLG) substrates using the DC sputtering method. An ultrathin Ag layer (3–9 nm) was subsequently deposited at room temperature (25 °C) using a low sputtering power of 50 W for 30–90 s.

Fabrication of the Sb_2Se_3 device—The solar cells were fabricated in the configuration SLG/Mo/Ag/Sb_2Se_3/CdS/i-ZnO/AZO/Al. A 700-nm Sb_2Se_3 layer as the light-absorbing layer was deposited via co-evaporation method on top of the Ag interlayer or directly on the Mo electrode layer on SLG. During deposition, the source tray was rapidly heated to $T_{sub} = 315$ °C, avoiding intentional selenization of the Mo back contact. A 50 nm CdS buffer layer was deposited using chemical bath deposition to complete the device.[46] To prevent Sb diffusion into the CdS layer during subsequent processing, a 2 nm ultrathin SnO_x layer was deposited onto the Sb_2Se_3 absorber layer via atomic layer deposition. The SnO_x layer was deposited in a custom-built ALD system operated at 100 °C, using TDMASn as the Sn precursor (maintained at 45 °C) and ozone (O_3) as the oxidant. The chamber base pressure was stabilized at 3×10^{-3} Torr, with an additional 20 sccm Ar flow during deposition. Throughout the process, the Sb_2Se_3 substrates were positioned on a hot trap heated to 350 °C to ensure uniform thermal conditions. Fabrication of the solar cell stacks was completed by finally sputtering *i*-ZnO (50 nm) and AZO (300 nm) layers on top (a schematic diagram illustrating the device layer stacking see in Figure S1, Supporting Information). Finally, each sample was divided into 16 individual solar cells ($A = 0.185$ cm^2) by scribing, as described in our previous study.[47]

Characterization: Surface and cross-sectional images were obtained using field-emission scanning electron microscopy (FESEM; Hitachi SU8020). The surface roughness of the films was determined from 3D surface topography images obtained by AFM (n-Tracer; NanoFocus Co.) in an ambient environment. XRD (Empyrean, PANalytical Co.) was performed using Cu Kα radiation

© 2026 The Author(s). *Energy & Environmental Materials* published by John Wiley & Sons Australia, Ltd on behalf of Zhengzhou University.

25750356, 0, Downloaded from https://onlinelibrary.wiley.com/doi/10.1002/eem2.70322 by Daegu Gyeongbuk Institute Of, Wiley Online Library on [09/04/2026]. See the Terms and Conditions (https://onlinelibrary.wiley.com/terms-and-conditions) on Wiley Online Library for rules of use; OA articles are governed by the applicable Creative Commons License

(λ = 0.15406 nm) to analyze the crystal structure. XPS was performed using an ESCALAB 250Xi spectrometer (Thermo Fisher Scientific) with a monochromatic Al Kα X-ray source, and charge correction was applied with reference to the C 1 s peak at 284.6 eV. UPS (Thermo Scientific K-Alpha) was used to determine the energy band positions of the Sb_2Se_3 absorbers. TRPL measurements were performed using a confocal microscope (MicroTime-200; PicoQuant, Germany). The lifetime measurements were conducted at the Korea Basic Science Institute (KBSI), Daegu. A single-mode pulsed diode laser (wavelength: 470 nm; pulse width: ∼30 ps) was used as the excitation source, operated at an average power of ∼6 μW (repetition rate: 2 MHz) for the Sb_2Se_3 device and ∼250 μW (repetition rate: 40 MHz) for the Sb_2Se_3 film. The setup included a dichroic mirror (490 DCXR, AHF), long-pass filter (HQ500lp, AHF), 150 μm pinhole, long-pass filter (FEL0900, Thorlabs), and single-photon avalanche diode (PDM series, MPD) to collect emissions from the samples. A 40× air objective (NA 0.95) was used for excitation. Photon counts were recorded using a time-correlated single-photon counting system (PicoHarp-300, PicoQuant GmbH, Germany). TRPL lifetime images (200 × 200 pixels) were recorded in time-tagged, time-resolved (TTTR) data acquisition mode. PL decay curves were fitted using an exponential function in the Symphotime-64 software. DFT calculations were performed at the HSE06-D3(BJ) level to investigate the effect of Ag incorporation under Se-rich growth conditions. The elemental distribution was analyzed using time-of-flight secondary ion mass spectrometry (TOF-SIMS; IONTOF, Germany). STEM-EDS was used for elemental mapping. Current–voltage curves were recorded under simulated AM 1.5G illumination at 100 mW cm^{-2} (1 sun) using a 94022A solar simulator (Newport Co.). The external quantum efficiency (EQE) spectra were obtained using EQE equipment (McScience) equipped with an Xe lamp. The power conversion efficiencies were determined without antireflection coatings or post-deposition treatments. To identify the acceptor defect energy levels and densities, AS was performed in the temperature range of 120–300 K using an E4980A LCR meter (Agilent Co.) with frequencies between 20 Hz and 2 MHz. Arrhenius plots of the inflection points of the AS curves were used to investigate the defect energy levels of the Sb_2Se_3 absorber layers. C–V and drive-level capacitance profiling (DLCP) measurements were conducted using an LCR meter (E4980A, Agilent) to calculate the space charge width and carrier density.

Acknowledgements

V.-Q.H. and J.L. contributed equally to this work. This research was supported by grants from the Korea Institute for Advancement of Technology (KIAT), funded by the Korean government (MOTIE) (No. P0024567), and the National Research Foundation of Korea (NRF), funded by the Korean government (MSIT) (Nos. RS-2025-02315803, RS-2023-NR076874). This work was also supported by the Inno-CORE program and the DGIST R&D programs, funded by the Korean government (MSIT) (Nos. 1.260007.01, 26-ET-01, 25-PCOE-01).

Conflicts of Interest

The authors declare no competing financial interest.

Data Availability Statement

The data that support the findings of this study are available from the corresponding author upon reasonable request.

Supporting Information

Supporting Information is available from the Wiley Online Library or from the author.

Keywords

Ag incorporation, $AgSbSe_2$, defect passivation, phase transitions, Sb_2Se_3, thermal co-evaporation

Received: November 21, 2025
Revised: January 9, 2026
Published online: January 22, 2026

[1] A. Mavlonov, T. Razykov, F. Raziq, J. Gan, J. Chantana, Y. Kawano, T. Nishimura, H. Wei, A. Zakutayev, T. Minemoto, *Sol. Energy* **2020**, *201*, 227.
[2] C. Chen, D. C. Bobela, Y. Yang, S. Lu, K. Zeng, C. Ge, B. Yang, L. Gao, Y. Zhao, M. C. Beard, *Front. Optoelectron.* **2017**, *10*, 18.
[3] S. Hadke, M. Huang, C. Chen, Y. F. Tay, S. Chen, J. Tang, L. Wong, *Chem. Rev.* **2021**, *122*, 10170.
[4] C. Chen, W. Li, Y. Zhou, C. Chen, M. Luo, X. Liu, K. Zeng, B. Yang, C. Zhang, J. Han, *Appl. Phys. Lett.* **2015**, *107*, 043905.
[5] X. Peng, Z. Ma, Z. He, R. Tang, J. Li, S. Sheng, T. Wu, Y. Hu, Z. Cai, Z. Jiang, *Adv. Funct. Mater.* **2025**, 35, 2503314.
[6] S. Rühle, *Sol. Energy* **2016**, *130*, 139.
[7] Y. Zhou, M. Leng, Z. Xia, J. Zhong, H. Song, X. Liu, B. Yang, J. Zhang, J. Chen, K. Zhou, *Adv. Energy Mater.* **2014**, *4*, 1301846.
[8] X. Liu, J. Chen, M. Luo, M. Leng, Z. Xia, Y. Zhou, S. Qin, D.-J. Xue, L. Lv, H. Huang, *ACS Appl. Mater. Interfaces* **2014**, *6*, 10687.
[9] M. N. Tran, M. Moreau, A. Addad, A. Teurtrie, T. Roland, V. De Waele, M. Dewitte, L. Thomas, G. Levêque, C. Dong, *ACS Appl. Mater. Interfaces* **2024**, *16*, 14852.
[10] M. N. Tran, A. Skorynina, A. Addad, A. Fadel, K. B. Tayeb, L. Karmazin, L. Thomas, M. Corda, Y. Wisse, O. Vovk, *Appl. Catal. B* **2025**, *363*, 124834.
[11] Z. Wang, S. Bae, M. Baljozović, P. Adams, D. Yong, E. Service, T. Moehl, W. Niu, S. D. Tilley, *ACS Catal.* **2024**, *14*, 9877.
[12] Y. Li, Y. Zhou, J. Luo, W. Chen, B. Yang, X. Wen, S. Lu, C. Chen, K. Zeng, H. Song, *RSC Adv.* **2016**, *6*, 87288.
[13] P. Adams, F. Creazzo, T. Moehl, R. Crockett, P. Zeng, Z. Novotny, S. Luber, W. Yang, S. D. Tilley, *J. Mater. Chem. A* **2023**, *11*, 8277.
[14] J. Hwang, Y. Cho, D. Shin, I. Jeong, J. H. Park, J.-S. Cho, J. Gwak, J. H. Yun, K. Han, H. S. Chang, *J. Alloys Compd.* **2021**, *886*, 161193.
[15] M. Xu, S. Yan, T. Liang, J. Jia, S. Yuan, D. Kou, Z. Zhou, W. Zhou, Y. Qi, Y. Meng, *J. Energy Chem.* **2025**, *100*, 59.
[16] Y. Ma, B. Tang, W. Lian, C. Wu, X. Wang, H. Ju, C. Zhu, F. Fan, T. Chen, *J. Mater. Chem. A* **2020**, *8*, 6510.
[17] A. Kuruvilla, M. Francis, M. Lakshmi, *AIP Conf. Proc.* **2019**, *2162*, 020080.
[18] S. Gautam, A. Thakur, S. Tripathi, N. Goyal, *J. Non-Cryst. Solids* **2007**, *353*, 1315.
[19] W. Dong, M. Krbal, J. Kalikka, X. Y. Chin, B. Gholipour, C. Soci, P. Fons, K. V. Mitrofanov, L. Chen, R. E. Simpson, *Thin Solid Films* **2016**, *616*, 80.
[20] J. Capistran-Martinez, M. S. Nair, P. K. Nair, *Phys. Status Solidi A Appl. Res.* **2021**, *218*, 2100058.
[21] A. Nadukkandy, S. Shaji, D. A. Avellaneda, J. A. Aguilar-Martinez, B. Krishnan, *J. Alloys Compd.* **2023**, *942*, 169072.
[22] C. Guo, X. Liang, T. Liu, Y. Liu, L. Yang, W. Lai, R. Schropp, D. Song, Y. Mai, Z. Li, *Sol. RRL* **2020**, *4*, 2000054.
[23] P. Erslev, G. M. Hanket, W. N. Shafarman, D. J. Cohen, *MRS Online Proc. Libr.* **2009**, *1165*, 1165-M1101-1107.
[24] A. J. C. M. Prot, M. Melchiorre, T. Schaaf, R. G. Poeira, H. Elanzeery, A. Lomuscio, S. Oueslati, A. Zelenina, T. Dalibor, G. Kusch, *Sol. RRL* **2024**, *8*, 2400208.
[25] P. Myagmarsereejid, M. Ingram, M. Batmunkh, Y. L. Zhong, *Small* **2021**, *17*, 2100241.
[26] M. Isik, O. Surucu, T. Bektas, M. Parlak, *Opt. Mater.* **2025**, *167*, 117362.
[27] H. El-Zahed, *Thin Solid Films* **1994**, *238*, 104.
[28] A. Kuruvilla, M. Francis, M. Lakshmi, *Arab. J. Sci. Eng.* **2023**, *48*, 8115.
[29] L. Guo, B. Zhang, Y. Qin, D. Li, L. Li, X. Qian, F. Yan, *Sol. RRL* **2018**, *2*, 1800128.
[30] L. Guo, P. S. Shinde, Y. Ma, L. Li, S. Pan, F. Yan, *Sol. RRL* **2020**, *4*, 1900442.

© 2026 The Author(s). *Energy & Environmental Materials* published by John Wiley & Sons Australia, Ltd on behalf of Zhengzhou University.

25750356, 0, Downloaded from https://onlinelibrary.wiley.com/doi/10.1002/eem2.70322 by Daegu Gyeongbuk Institute Of, Wiley Online Library on [09/04/2026]. See the Terms and Conditions (https://onlinelibrary.wiley.com/terms-and-conditions) on Wiley Online Library for rules of use; OA articles are governed by the applicable Creative Commons License

[31] Z. Li, X. Liang, G. Li, H. Liu, H. Zhang, J. Guo, J. Chen, K. Shen, X. San, W. Yu, *Nat. Commun.* **2019**, *10*, 125.
[32] J. Otavio Mendes, A. Merenda, K. Wilson, A. Fraser Lee, E. Della Gaspera, J. van Embden, *Small* **2024**, *20*, 2302721.
[33] Y. Asada, *J. Appl. Phys.* **1985**, *58*, 3162.
[34] Y. Yin, C. Jiang, Y. Ma, R. Tang, X. Wang, L. Zhang, Z. Li, C. Zhu, T. Chen, *Adv. Mater.* **2021**, *33*, 2006689.
[35] S. Li, H. Shen, J. Chen, Y. Jiang, L. Sun, A. Raza, Y. Xu, *J. Mater. Sci. Mater. Electron.* **2019**, *30*, 19871.
[36] R. Sharma, S. Sharma, P. Kumar, R. Chander, R. Thangaraj, M. Mian, *Mater. Sci.-Pol.* **2016**, *34*, 794.
[37] Y. T. Alharbi, F. Alam, A. Salhi, M. Missous, D. J. Lewis, *Sci. Rep.* **2021**, *11*, 3053.
[38] C. Diliegros-Godines, J. Santos Cruz, N. Mathews, M. Pal, *J. Mater. Sci.* **2018**, *53*, 11562.
[39] S. Hussain, J. Chae, K. Akbar, D. Vikraman, L. Truong, B. A. Naqvi, Y. Abbas, H.-S. Kim, S.-H. Chun, G. Kim, *Nano* **2019**, *9*, 1460.
[40] T. K. Shivasharma, L. K. Bommineedi, B. R. Sankapal, *Inorg. Chem. Commun.* **2022**, *135*, 109083.
[41] W. Yang, S. Lee, H.-C. Kwon, J. Tan, H. Lee, J. Park, Y. Oh, H. Choi, J. Moon, *ACS Nano* **2018**, *12*, 11088.
[42] E. Cho, S.-J. Sung, K.-J. Yang, J. Lee, V.-Q. Hoang, B. Kadiri-English, D.-K. Hwang, J.-K. Kang, D.-H. Kim, *J. Mater. Chem. A* **2025**, *13*, 8507.
[43] C. Chen, J. Tang, *ACS Energy Lett.* **2020**, *5*, 2294.
[44] Y. Zhao, S. Wang, C. Li, B. Che, X. Chen, H. Chen, R. Tang, X. Wang, G. Chen, T. Wang, *Energy Environ. Sci.* **2022**, *15*, 5118.
[45] S. Kim, J. Lee, D.-H. Son, W. H. Kim, S.-J. Sung, D.-K. Hwang, T. E. Hong, N. Otgontamir, E. Enkhbayar, T.-H. Lee, *Energy Environ. Sci.* **2024**, *17*, 8609.
[46] H. Yoo, H. Van Quy, I. Lee, S. T. Jo, T. E. Hong, J. Kim, D. H. Yoo, J. Shin, W. Commerell, D. H. Kim, *Energy Environ. Mater.* **2024**, *7*, e12765.
[47] V.-Q. Hoang, D.-H. Jeon, S.-Y. Kim, J. Lee, D.-H. Son, K.-J. Yang, J.-K. Kang, S.-J. Sung, D.-K. Hwang, D.-H. Kim, *J. Sci. Adv. Mater. Devices* **2024**, *9*, 100665.

© 2026 The Author(s). *Energy & Environmental Materials* published by John Wiley & Sons Australia, Ltd on behalf of Zhengzhou University.

25750356, 0, Downloaded from https://onlinelibrary.wiley.com/doi/10.1002/eem2.70322 by Daegu Gyeongbuk Institute Of, Wiley Online Library on [09/04/2026]. See the Terms and Conditions (https://onlinelibrary.wiley.com/terms-and-conditions) on Wiley Online Library for rules of use; OA articles are governed by the applicable Creative Commons License